

# Fine-tuning deep learning model parameters for improved super-resolution of dynamic MRI with prior-knowledge

Chompunuch Sarasaen<sup>a,b,c,\*</sup>, Soumick Chatterjee<sup>a,c,d,e,\*</sup>, Mario Bretkopf<sup>a,c</sup>, Georg Rose<sup>b,c</sup>, Andreas Nürnberger<sup>d,e,g</sup>, Oliver Speck<sup>a,c,f,g,h</sup>

<sup>a</sup>Biomedical Magnetic Resonance, Otto von Guericke University Magdeburg, Germany

<sup>b</sup>Institute for Medical Engineering, Otto von Guericke University Magdeburg, Germany

<sup>c</sup>Research Campus STIMULATE, Otto von Guericke University Magdeburg, Germany

<sup>d</sup>Faculty of Computer Science, Otto von Guericke University Magdeburg, Germany

<sup>e</sup>Data and Knowledge Engineering Group, Otto von Guericke University Magdeburg, Germany

<sup>f</sup>German Center for Neurodegenerative Disease, Magdeburg, Germany

<sup>g</sup>Center for Behavioral Brain Sciences, Magdeburg, Germany

<sup>h</sup>Leibniz Institute for Neurobiology, Magdeburg, Germany

## Abstract

Dynamic imaging is a beneficial tool for interventions to assess physiological changes. Nonetheless during dynamic MRI, while achieving a high temporal resolution, the spatial resolution is compromised. To overcome this spatio-temporal trade-off, this research presents a super-resolution (SR) MRI reconstruction with prior knowledge based fine-tuning to maximise spatial information while preserving high temporal resolution of dynamic MRI. An U-Net based network with perceptual loss is trained on a benchmark dataset and fine-tuned using one subject-specific static high resolution MRI as prior knowledge to obtain high resolution dynamic images during the inference stage. 3D dynamic data for three subjects were acquired with different parameters to test the generalisation capabilities of the network. The method was tested for different levels of in-plane undersampling for dynamic MRI. The reconstructed dynamic SR results after fine-tuning showed higher similarity with the high resolution ground-truth, while quantitatively achieving statistically significant improvement. The average SSIM of the lowest resolution experimented during this research (6.25 % of the k-space) before and after fine-tuning were  $0.939 \pm 0.008$  and  $0.957 \pm 0.006$  respectively. This could theoretically result in an acceleration factor of 16, which can potentially be acquired in less than half a second. The proposed approach shows that the super-resolution MRI reconstruction with prior-information can alleviate the spatio-temporal trade-off in dynamic MRI, even for high acceleration factors.

**Keywords:** super-resolution, dynamic MRI, prior knowledge, fine-tuning, patch-based super-resolution, deep learning

## 1. Introduction

Magnetic Resonance Imaging (MRI) is in clinical use for a few decades with the advantage of non-ionising radiation, non-invasiveness and an excellent soft tissue contrast. Considering the clear visibility of tumours because of its high soft tissue contrast, together with real-time supervision (e.g. thermometry), MRI is a promising tool for interventions. The visualisation of lesions, as well as the needle paths, have to be acquired prior to any interventional procedures, so-called a planning scan or a preinterventional MR imaging (Mahnken et al., 2009). Furthermore, in MR-guided interventions, such as liver biopsy, it is necessary to continuously acquire data and reconstruct a series of images during interventions, in order to examine dynamic movements of internal organs Bernstein et al. (2004). A clear interpretable visualisation of the target lesion, surrounding tissues including risk structures is crucial during interventions. In order to achieve a high temporal resolution during dynamic MRIs, because of the inherently slow speed

of image acquisition, the amount of data to be acquired has to be reduced - which may result in loss of spatial resolution. Although there are a number of techniques dealing with this spatio-temporal trade-off (Tsao et al., 2003; Lustig et al., 2006, 2007; Jung et al., 2009), their speed of reconstruction creates a hindrance for real-time or near real-time imaging. Therefore, a compromise between spatial and temporal resolution is inevitable during real-time MRIs and needs to be mitigated.

The so-called super-resolution (SR) algorithms aim to restore images with high spatial resolution from the corresponding low resolution images. SR approaches have been widely used for various applications (Zhang et al., 2014; Sajjadi et al., 2017), including for super-resolution of MRIs (SR-MRI) (Van Reeth et al., 2012; Plenge et al., 2012; Isaac and Kulkarni, 2015). Furthermore, deep learning based super-resolution reconstruction has been substantiated in recent times to be a successful tool for SR-MRI (Zeng et al., 2018; He et al., 2020), including for dynamic MRIs (Qin et al., 2018; Lyu et al., 2020). However, most deep learning based methods need large training data sets and finding such training data – matching with the data of the real-time acquisition that needs to be reconstructed in terms

\*C. Sarasaen and S. Chatterjee contributed equally to this work.

of contrast and sequence – can be a challenging task. Using a training set significantly different than the test set can produce results of poor quality (Wang and Deng, 2018; Wilson and Cook, 2020). Several techniques have been used to deal with the problem of small datasets in deep learning, such as data augmentation (Perez and Wang, 2017) and synthetic data generation (Lateh et al., 2017; Frid-Adar et al., 2018). However, these methods rely on artificially modifying the data to increase the size of the dataset. Patch-based training can also help cope with the small dataset problem by splitting each data into smaller patches. This can effectively increase the number of samples in the dataset without artificially modifying the data (Frid-Adar et al., 2017). The patch-based super-resolution (PBSR) techniques learn the mapping function from given corresponding pairs of high resolution and low resolution image patches (Yang et al., 2014).

This study proposes a PBSR reconstruction, aiming at addressing the problem of the lack of large abdominal datasets for training. This research intends to improve deep learning based super-resolution of dynamic MR images by incorporating prior images (planning scan). The network was trained on a publicly available abdominal dataset of 40 subjects, acquired using different sequences than the dynamic MR that is to be reconstructed. After that, the network was fine-tuned using a high resolution prior planning scan of the same subject as the dynamic acquisition.

### 1.1. Related works

Super-resolution approaches have been employed for a wide variety of tasks, such as computer vision (Shi et al., 2016; Dong et al., 2016; Sajjadi et al., 2017), remote sensing (Zhang et al., 2014; Ran et al., 2020), face-related tasks (Tappen and Liu, 2012; Yu et al., 2018) and medical applications (Isaac and Kulkarni, 2015; Huang et al., 2017). Deep learning based methods have been widely used in recent times for performing super-resolution (Dong et al., 2014; Zhu et al., 2014; Dong et al., 2016; Ran et al., 2020). Moreover, deep learning based techniques have been proven to be a successful tool for numerous applications in the field of MRI, including for performing MR reconstruction (Wang et al., 2016; Hyun et al., 2018; Hammernik et al., 2018; Chatterjee et al., 2019) and for SR-MRI (Zeng et al., 2018; Liu et al., 2018; Chaudhari et al., 2018; He et al., 2020). Different deep learning based SR-MRI ideas have been proposed for static brain MRI (Huang et al., 2017; Tanno et al., 2017; Pham et al., 2017; Zeng et al., 2018; Liu et al., 2018; Chen et al., 2018; Deka et al., 2020; Gu et al., 2020). Furthermore, deep learning based methods have additionally been shown to tackle the spatio-temporal trade-off (Liang et al., 2020), also for dynamic cardiac MR reconstruction (Qin et al., 2018; Lyu et al., 2020).

Single-image super-resolution techniques are classified into the groups of prediction-based, edge-based, image statistical and patch-based methods (Yang et al., 2014). PBSR can overcome the need of large training datasets as the actual training is done using patches, rather than on whole images. The PBSR methods have been applied to different tasks, including applications in medical imaging (Manjón et al., 2010; Rousseau

et al., 2010; Zhang et al., 2012; Coupé et al., 2013; Jain et al., 2017). By employing PBSR, the reconstruction procedure can be driven to cope with the limitation of available training abdominal MR data (Tang and Shao, 2016; Misra et al., 2020).

The U-Net (Ronneberger et al., 2015) model, which was originally proposed for image segmentation, over the past few years has been proven to solve various inverse problems as well (Hyun et al., 2018; Iqbal et al., 2019; Ghodrati et al., 2019). Iqbal et al. (2019) developed an U-Net based architecture for SR reconstruction of MR spectroscopic images. Hyun et al. (2018) reconstructed MRI utilising a 2D U-Net from zero-filled data, undersampled using uniform Cartesian sampling (GRAPPA-like) with a dense k-space centre. Ghodrati et al. (2019) employed a U-Net model to test the performance of this network structure for cardiac MRI reconstruction. Due to the promising results shown in the papers mentioned earlier, the current paper proposed a 3D U-Net (Çiçek et al., 2016) based architecture for performing SR-MRI for abdominal dynamic images.

Transfer learning is a technique for re-proposing or adapting a pre-trained model with fine-tuning (Bengio et al., 2017). With transfer learning, the network weights learned from one task can be used as pre-trained weights for another task, and then the network is trained (fine-tuned) for the new task. It has been widely used in data mining and machine learning (Dai et al., 2007; Li et al., 2009; Choi et al., 2017; Lee et al., 2018). Transfer learning can address the issue of having insufficient training data (Zhao, 2017; Kim et al., 2020). The fine-tuning process is known to improve the network’s performance and can help to converge in less training epochs with smaller datasets (Pan and Yang, 2009). One of the main research inquiries of applying transfer learning is “what to transfer”. This current study thereby, utilises the specific knowledge of priors from a static planing image, which is usually acquired earlier to an interventional procedure. The incorporation of priors is meant to constrain anatomical structures in the fine-tuning process and to improve the data fidelity term in the regularisation process.

To determine the reconstruction error during training a deep learning model, between the model’s prediction and the corresponding ground-truth images, the selection of a loss function is crucial. Pixel-based loss functions such as mean squared error (L2 loss) are commonly used for SR, however, in terms of perceptual quality, it often generates too smooth results which is caused due to the loss of high-frequency details (Wang et al., 2003, 2004; Johnson et al., 2016; Ledig et al., 2017). Perceptual loss has shown potential to achieve high-quality images for image transformation tasks such as style transfer (Johnson et al., 2016; Gatys et al., 2016). For MRI reconstruction, Ghodrati et al. Ghodrati et al. (2019) have shown a comparative study of loss functions, such as perceptual loss (using VGG-16 as perceptual loss network), pixel-based loss (L1 and L2) and patch-wise structural dissimilarity (Dssim), for deep learning based cardiac MR reconstruction. They found that the results of the perceptual loss outperformed the other loss functions. Hence, in this work a combination of perceptual loss network with the mean absolute error (MAE) as the loss function was used, which is explained in section 2.3.1.

### 1.2. Problem statement

Given a low resolution image  $I_{LR}$  and a corresponding high resolution image  $I_{HR}$ , the reconstructed high resolution image  $\hat{I}_{HR}$  can be recovered from a super-resolution reconstruction using the following equation (Wang et al., 2020):

$$\hat{I}_{HR} = F(I_{LR}; \theta) \quad (1)$$

where  $F$  denotes the super-resolution model that maps the image counterparts and  $\theta$  denotes the parameters of  $F$ . The SR image reconstruction is an ill-posed problem, a network model can be trained to solve the objective function:

$$\hat{I}_{HR} = \arg \min \mathcal{L}(\hat{I}_{HR}, I_{HR}) + \lambda R(I_{LR}) \quad (2)$$

where the  $\mathcal{L}(\hat{I}_{HR}, I_{HR})$  denotes the loss function between the approximated HR image  $\hat{I}_{HR}$  and ground-truth image  $I_{HR}$ ,  $\lambda R(I_{LR})$  is a regularisation term and  $\lambda$  denotes the trade-off parameter.

### 1.3. Contributions

This paper presents a method to incorporate prior knowledge in deep-learning based super-resolution and its application in dynamic MRI. The main contributions are as follows:

- This paper addresses the trade-off between the spatial and temporal resolution of dynamic MRI by incorporating a static high resolution scan as prior knowledge.
- A 3D U-Net model was first trained for the task of SR-MRI on a benchmark dataset and was fine-tuned using a subject-specific prior planning scan.
- This paper further tackles the problem of the lack of high-resolution dynamic MRI for training in two ways:
  - By using a static benchmark dataset for training, having different contrasts and resolutions than the target dynamic MRI; followed by fine-tuning using one static planning scan
  - By patch-based super-resolution training and fine-tuning
- To achieve realistic super-resolved images, perceptual loss was used as the loss function for training and fine-tuning the model, which was calculated using a 3D perceptual loss network pre-trained on MR images.

## 2. Methodology

This paper proposes a framework of patch-based MR super-resolution based on U-Net, incorporating prior knowledge. The framework can be divided into three stages: main training, fine-tuning and inference. The U-Net model was initially trained with a benchmark dataset for main-training and then was fine-tuned using a subject-specific prior static scan. Finally in the inference stage, high resolution dynamic MRIs were reconstructed from low resolution scans. This chapter starts with the

description of various datasets used in this research, then explains the network architecture followed by the implementation and training, finally explains the metrics used for evaluation.

### 2.1. Data

In this work, 3D abdominal MR volumes were artificially downsampled in-plane using MRUnder (Chatterjee, 2020)<sup>1</sup> pipeline to simulate low resolution datasets. The low resolution data was generated by performing undersampling in-plane (phase-encoding and read-out direction) by taking the centre of k-space without zero-padding. The CHAOS challenge dataset (Kavur et al., 2020) (T1-Dual; in- and opposed-phase images) was used for the main training. High resolution 3D static (breath-hold) and 3D "pseudo"-dynamic (free-breathing) scans for 10 time-points (TP) using T1w FLASH sequence were acquired for fine-tuning and inference respectively. Each time-point of the dynamic acquisition was treated as separate 3D Volume. Three healthy subjects were scanned with the same sequence but with different parameters on a 3T MRI (Siemens Magnetom Skyra). This aims to test the generalisation of the network. For each subject, the 3D static and the 3D dynamic scans were acquired in different sessions using the same sequences and parameters. The sequence parameters of the various datasets have been listed in Table 1. The CHAOS dataset (for main training), the 3D static scans (for fine-tuning) and the 3D dynamic scans (for inference) were artificially downsampled for three different levels of image resolution, by taking 25%, 10% and 6.25% of the k-space centre, resulting in MR acceleration factor of 2, 3 and 4 respectively (considering undersampling only in the phase-encoding direction). This can be accelerated theoretically to a factor of 4, 9 and 16 respectively considering the amount of data used for the SR reconstruction. The effective resolutions and the roughly estimated acquisition times of the low resolution images were calculated from the corresponding high-resolution images, are reported in Table 2. The acquisition times were calculated as  $AcqTime = PE_n \times TR \times S_m$ , where  $PE_n$  is the number of phase-encoding steps,  $TR$  is the repetition time, and  $S_m$  is the number of slices. Phase/slice oversampling, phase/slice resolutions and GRAPPA factor were taken into account while calculating  $PE_n$ . The low resolution images served as the input to the network and were compared against the high resolution ground-truth images.

### 2.2. Network Architecture

Fig 1 portrays the proposed network architecture. In this work, a 3D U-Net based model (Ronneberger et al., 2015; Çiçek et al., 2016; Sarasaen et al., 2020) with perceptual loss network (Chatterjee et al., 2020) was employed for super-resolution reconstruction. The U-Net architecture consists of two main paths; contracting (encoding) and expanding (decoding). The contracting path consists of three blocks, each comprises of two convolutional layers and a ReLU activation function. The expanding path also consists of three blocks, but con-

<sup>1</sup>MRUnder on Github: <https://github.com/soumickmj/MRUnder>

Table 1: MRI acquisition parameters CHAOS dataset and subject-wise 3D dynamic scans. Static scans were performed using the same subject-wise sequence parameters as the dynamic scans for one time-point (TP), acquired at a different session.

|                             | CHAOS<br>(40 Subjects)   | Subject 1              | Subject 2              | Subject 3              |
|-----------------------------|--|------------------------|------------------------|------------------------|
| Sequence                    | T1 Dual In-Phase<br>& Opposed-Phase  | T1w Flash 3D           | T1w Flash 3D           | T1w Flash 3D           |
| Resolution                  | 1.44 x 1.44 x 5 -<br>2.03 x 2.03 x 8 $mm^3$                                  | 1.09 x 1.09 x 4 $mm^3$ | 1.09 x 1.09 x 4 $mm^3$ | 1.36 x 1.36 x 4 $mm^3$ |
| FOV x, y, z                 | 315 x 315 x 240 -<br>520 x 520 x 280 $mm^3$                                  | 280 x 210 x 160 $mm^3$ | 280 x 210 x 160 $mm^3$ | 350 x 262 x 176 $mm^3$ |
| Encoding matrix             | 256 x 256 x 26 -<br>400 x 400 x 50   | 256 x 192 x 40         | 256 x 192 x 40         | 256 x 192 x 44         |
| Phase/Slice oversampling    | -  | 10/0 %                 | 10/0 %                 | 10/0 %                 |
| TR/TE                       | 110.17 - 255.54 ms /<br>4.60 - 4.64 ms (In-Phase)<br>2.30 ms (Opposed-Phase) | 2.34/0.93 ms           | 2.34/0.93 ms           | 2.23/0.93 ms           |
| Flip angle                  | 80°  | 8°                     | 8°                     | 8°                     |
| Bandwidth                   | -  | 975 Hz/Px              | 975 Hz/Px              | 975 Hz/Px              |
| GRAPPA factor               | None   | 2                      | None                   | None                   |
| Phase/Slice partial Fourier | -  | Off/Off                | Off/Off                | Off/Off                |
| Phase/Slice resolution      | -  | 75/65 %                | 75/65 %                | 50/64 %                |
| Fat suppression             | -  | None                   | On                     | On                     |
| Time per TP                 | -  | 5.53 sec               | 11.76 sec              | 8.01 sec               |

Table 2: Effective resolutions and estimated acquisition times (per TP) of the dynamic and static datasets after performing different levels of artificial undersampling.

|                              | Subject 1                |                        | Subject 2                |                        | Subject 3                |                        |
|------------------------------|--------------------------|------------------------|--------------------------|------------------------|--------------------------|------------------------|
|                              | Resolution<br>( $mm^3$ ) | Acq. Time<br>( $sec$ ) | Resolution<br>( $mm^3$ ) | Acq. Time<br>( $sec$ ) | Resolution<br>( $mm^3$ ) | Acq. Time<br>( $sec$ ) |
| High Resolution Ground-truth | 1.09 x 1.09 x 4          | 4.81                   | 1.09 x 1.09 x 4          | 9.61                   | 1.36 x 1.36 x 4          | 6.62                   |
| 25% of k-space               | 2.19 x 2.19 x 4          | 1.22                   | 2.19 x 2.19 x 4          | 2.43                   | 2.73 x 2.73 x 4          | 1.65                   |
| 10% of k-space               | 3.50 x 3.50 x 4          | 0.47                   | 3.50 x 3.50 x 4          | 0.94                   | 4.38 x 4.38 x 4          | 0.66                   |
| 6.25% of k-space             | 4.38 x 4.38 x 4          | 0.28                   | 4.38 x 4.38 x 4          | 0.56                   | 5.47 x 5.47 x 4          | 0.42                   |

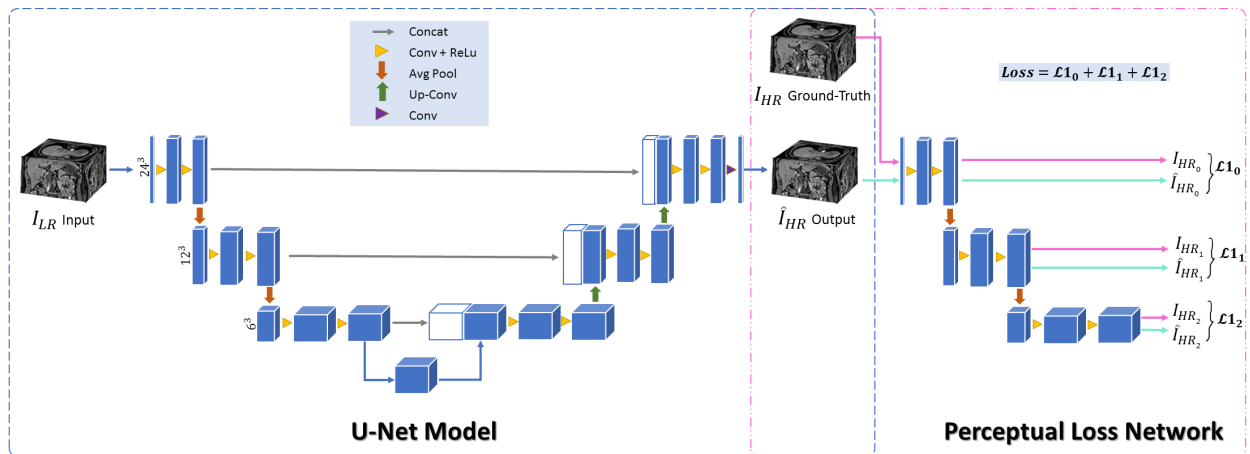


Figure 1: The proposed network Architecture.



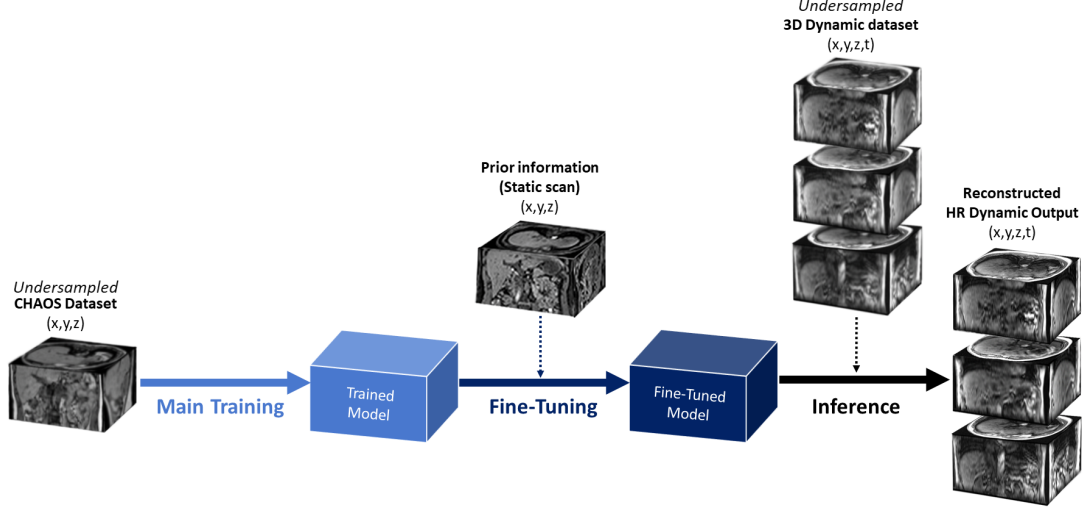


Figure 2: Method Overview.

volutional transpose layers were used instead of the convolutional layers. The training was performed using 3D patches of the volumes, with a patch size of  $24^3$ . U-Net model requires the same size for input and output images, therefore, the input images were interpolated using trilinear interpolation before supplying them to the network. Patch-based training may result in patching artefacts during inference. To remove these artefacts, the inference was performed with a stride of one and the overlapped portions were averaged after reconstruction.

### 2.3. Model Implementation and Network Training

Fig 2 shows the method overview. The main training was performed using 3D patches of the 80 volumes (40 subjects, in-phase and opposed-phase for each subject), with a patch size of  $24^3$  and a stride of 6 for the slice dimension and 12 for the other dimensions. After that, the network was fine-tuned using a single 3D static scan of the same subject from an earlier session, labelled as  $x,y,z,t$  in Fig 2. This static scan has the same resolution, contrast and volume coverage as the high resolution dynamic scan. The static and the dynamic scans were not co-registered to keep it similar to the real-life scenario and to keep the speed of inference fast. Fine-tuning and evaluations were performed with a patch size of  $24^3$  and a stride of one. The implementation was done using PyTorch (Paszke et al., 2019) and was trained using Nvidia Tesla V100 GPUs. The loss was minimised using the Adam optimiser with a learning rate of  $1e-4$ . The main training was performed for 200 epochs. The network was fine-tuned for only one epoch, using the planning scan with a lower learning rate ( $1e-6$ ).

#### 2.3.1. Perceptual Loss

Loss during the training and fine-tuning of the network was calculated with the help of perceptual loss (Johnson et al., 2016). The first three levels of the contraction path of a pre-trained (on 7T MRA scans, for vessel segmentation) frozen U-Net MSS model Chatterjee et al. (2020) were used as the

perceptual loss network (PLN) to extract features from the final super-resolved output of the model and the ground-truth images (refer to Fig.1). Typically VGG-16 trained on three-channel RGB non-medical images (ImageNet Dataset) is used as PLN, even while working with medical images (Ghodrati et al., 2019) as the PLN doesn't have to be trained on a similar dataset. In this research, the pre-trained network was chosen because it was originally trained on single-channel medical images, but of different contrast and organ; and it was hypothesised that using a network trained as such will be more suitable than a network trained on three-channel images. The extracted features from the model's output and from the ground-truth images were compared using mean absolute error (L1 loss). The losses obtained at each level for each feature were then added together and backpropagated.

### 2.4. Evaluation Metrics

To evaluate the quality of the reconstructed images against the ground-truth HR images, two of the most commonly used metrics for evaluating image quality were selected, namely the structural similarity index (SSIM)(Wang et al., 2004) and the peak signal-to-noise ratio (PSNR).

For perceptual quality assessment, the accuracy of the reconstructed images was compared to the ground truth using SSIM, which is based on the computations of luminance, contrast and structure terms between image  $x$  and  $y$ :

$$SSIM(x, y) = \frac{(2\mu_x\mu_y + c_1)(2\sigma_{xy} + c_2)}{(\mu_x^2 + \mu_y^2 + c_1)(\sigma_x^2 + \sigma_y^2 + c_2)} \quad (3)$$

where  $\mu_x, \mu_y, \sigma_x, \sigma_y$  and  $\sigma_{xy}$  are the local means, standard deviations, and cross-covariance for images  $x$  and  $y$ , respectively.  $c_1 = (k_1L)^2$  and  $c_2 = (k_2L)^2$ , where  $L$  is the dynamic range of the pixel-values,  $k_1 = 0.01$  and  $k_2 = 0.03$ .

Additionally, the performance of the model was measured statistically with PSNR. It is calculated via the mean-square

error (MSE) as:

$$PSNR = 10 \log_{10} \left( \frac{R^2}{MSE} \right) \quad (4)$$

where  $R$  is the maximum fluctuation in the input image.

### 3. Results and Discussion

Performance of the model was evaluated for three different levels of undersampling: by taking 25%, 10% and 6.25% of the k-space centre. The network was tested before and after fine-tuning using 3D dynamic MRI. The proposed approach was compared against the low resolution input, the traditional trilinear interpolation and finally against the most widely used technique in clinical MRIs - Fourier interpolation of the input (zero-filling k-space).

There was a noticeable improvement qualitatively and quantitatively while reconstructing low resolution data using the proposed method, even for only 6.25% of the k-space. Fig 3 shows the comparison qualitatively for the low resolution images by taking 25%, 10% and 6.25% of the k-space. Fig 4 portrays the comparison of the low resolution input for 6.25% of the k-space, the lowest resolution investigated during this study, with the SR result after fine-tuning over different time points. The SSIM maps were calculated against the high resolution ground-truth, which the respective SSIM value can be found on top of the image. Fig 5 illustrates the deviations of an example result from its corresponding ground-truth for two different regions of interest.

Additionally, for quantitative analysis, Table 3 displays the average and standard deviation (SD) of SSIM, PSNR and the SD of subtracted images for all time points for the dynamic datasets. Here, each time-point has been considered independent of each other as separate 3D volumes. To clearly show the distribution of the resultant metrics over all conditions and subjects, Fig 6 illustrates the SSIM and PSNR for different resolutions.

It can be observed that SR results after fine-tuning could alleviate the undersampling artefacts, which are still present in the SR results of the main training, even for relatively low resolution images like 10% and 6.25%. Consequently, the visibility of small details is improved. Fine-tuning with the planning scan helped in obtaining sharper images and achieving a better edge delineation. Furthermore, the statistical significance of the improvements in terms of SSIM achieved by the model after fine-tuning was evaluated using paired t-test and Wilcoxon signed-rank test. Separate tests were performed considering all the different resolutions together and also by considering each resolution separately. It was observed that the improvement was statistically significant in every evaluated scenario (p-values were always less than 0.001).

The acquisition time of high resolution 3D "pseudo"-dynamic reference data without parallel acquisition in this study was ten seconds and five seconds with GRAPPA factor two (Table 2). These are not sufficient for real-time or near real-time

applications and might lead to blurring in free-breathing subjects. This research shows the potential to acquire such volume with only minimal loss of spatial information in less than half a second.

The fine-tuning process took approximately eight hours to finish for each subject using the earlier mentioned setup (Section 2.3). Super-resolving each time-point took only a fraction of a second. The required time for fine-tuning and inference can further be reduced by reducing the patch-overlap (stride), though that might reduce the quality of the resultant super-resolved images. It can be further perceived that the network was able to produce results highly similar to the ground-truth (SSIM of 0.957) even while super-resolving 6.25% of k-space, which can make the acquisition 16 times faster. Combining this fast acquisition speed with the inference speed of the method, this study can be extended to be used for real-time or near real-time MRIs during interventions.

In the current study, only the centre of the k-space was used during undersampling, which results in loss of resolution without creating explicit image artefacts. Other undersampling patterns, such as variable density or GRAPPA-like uniform undersampling of higher spatial frequencies may be investigated in the future.

It should be noted that the static planning scans and the actual dynamic scans during interventions are typically acquired with different sequences, with planning scans having higher contrast and resolution than the dynamic scans. This study was conducted using the same sequence for static and dynamic scans, but different resolutions and positions (different scan session). An additional experiment was performed by fine-tuning using a volumetric interpolated breath-hold examination (VIBE) sequence as planing scan for one subject. Super-resolving the dynamic low-resolution images from 6.25% of the k-space resulted in 0.032 lower SSIM than using the identical sequence with higher resolution for fine-tuning. This may be a limitation of the current approach but requires further investigation.

### 4. Conclusion and Future Work

This research shows that fine-tuning with a subject-specific prior static scan can significantly improve the results of deep learning based super-resolution (SR) reconstruction. A 3D U-Net based model was trained with the help of perceptual loss to estimate the reconstruction error. The network model was initially trained using the CHAOS abdominal benchmark dataset and was then fine-tuned using a static high resolution prior scan. The model was used to obtain super-resolved high resolution 3D abdominal dynamic MRI from their corresponding low resolution images. Even though the network was trained using MRI sequences different than the reconstructed dynamic MRI, the SR results after fine-tuning showed higher similarity with the ground-truth images. The proposed method could overcome the spatio-temporal trade-off by improving the image resolution without compromising the speed of acquisition. This approach could be applied to real-time dynamic acquisitions, such as for interventional MRIs, because of the high speed of inference of deep learning models.

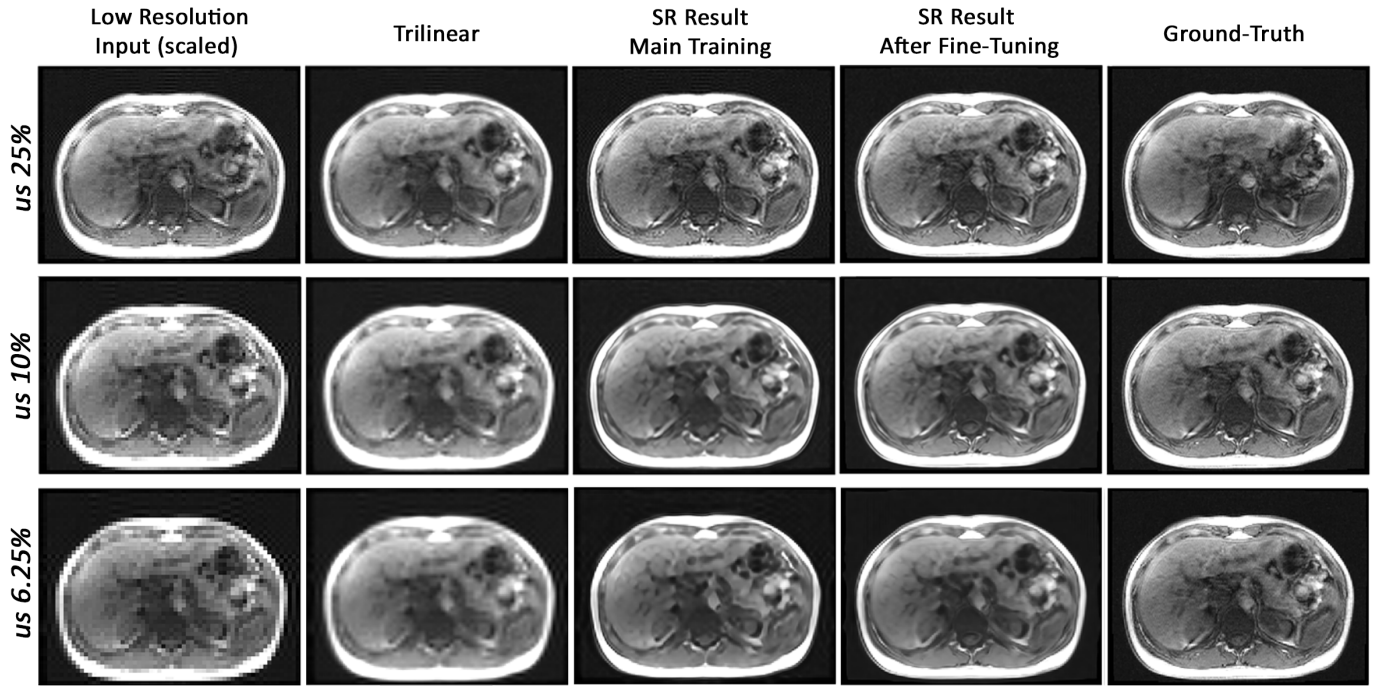


Figure 3: Comparative results of low resolution (25%, 10% and 6.25% of k-space) 3D Dynamic data of the same slice. From left to right: low resolution images (scaled-up), Interpolated input (Trilinear), super-resolution results of the main training (SR Results Main Training), super-resolution results after the fine-tune (SR After Fine-Tuning) and ground-truth images.

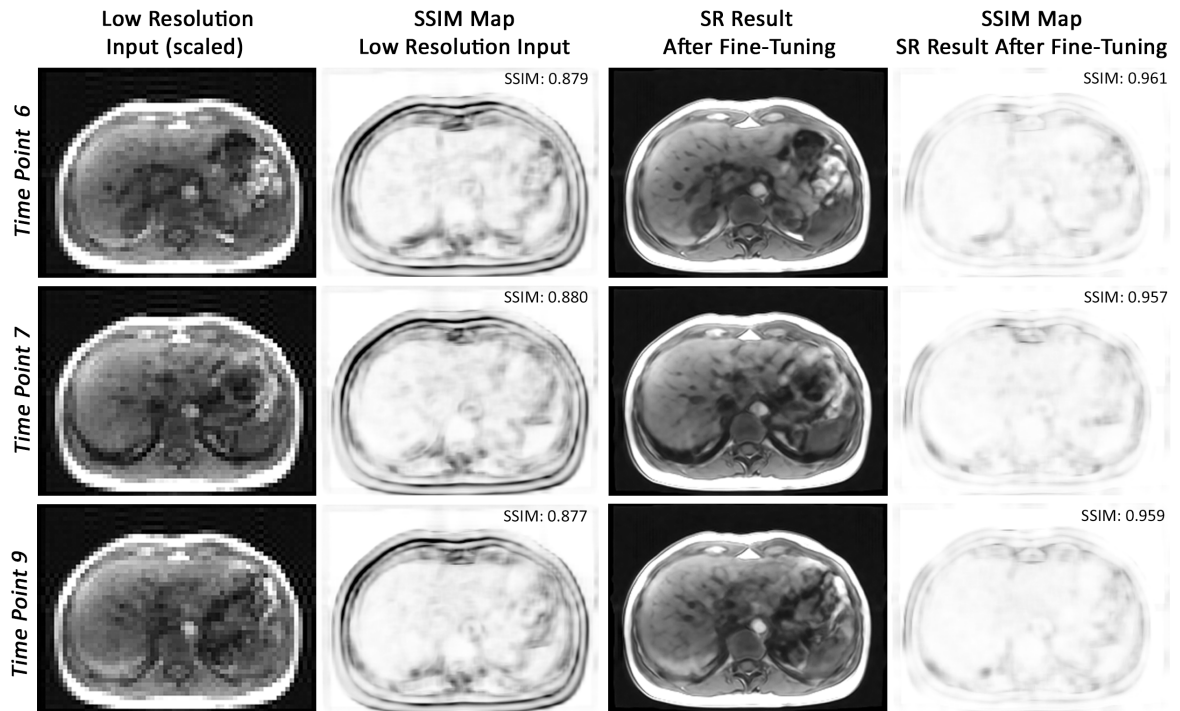


Figure 4: An example comparison of the low resolution input of the 6.25% of k-space with the super-resolution (SR) result after fine-tuning over three different time points, compared against the high resolution ground-truth using SSIM maps.

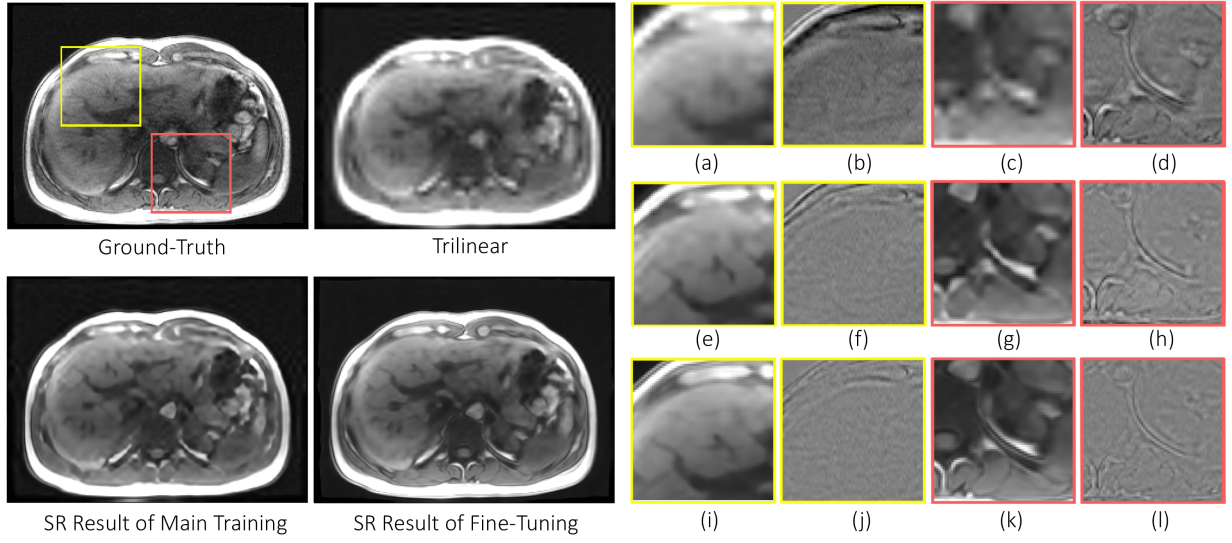


Figure 5: An example from the reconstructed results, compared against its ground-truth (GT) for low resolution images from 6.25% of k-space. From left to right, upper to lower: ground-truth, trilinear interpolation, SR result of main training and SR result after fine-tuning. For the yellow ROI, (a-b): trilinear interpolation and the difference image from GT, (e-f): SR result of the main training and the difference image from GT and (i-j): SR result after fine-tuning and the difference image from GT. The images on the right part are identical examples for the red ROI.

Table 3: The average and the standard deviation of SSIM, PSNR, and SD of difference images with ground-truth. The table shows the results of different resolutions.

| Data             | 25% of k-space |              |             | 10% of k-space |              |             | 6.25% of k-space |              |             |
|------------------|----------------|--------------|-------------|----------------|--------------|-------------|------------------|--------------|-------------|
|                  | SSIM           | PSNR         | diff SD     | SSIM           | PSNR         | diff SD     | SSIM             | PSNR         | diff SD     |
| Trilinear        | 0.964±0.005    | 37.680±1.770 | 0.013±0.002 | 0.906±0.007    | 33.148±1.780 | 0.022±0.004 | 0.872±0.011      | 31.504±1.786 | 0.026±0.005 |
| Zero-padded      | 0.977±0.013    | 37.980±4.078 | 0.064±0.011 | 0.926±0.009    | 31.844±2.260 | 0.067±0.013 | 0.888±0.012      | 29.803±2.147 | 0.069±0.015 |
| SR Main Training | 0.986±0.007    | 44.893±4.503 | 0.009±0.002 | 0.961±0.009    | 36.710±1.086 | 0.014±0.002 | 0.939±0.008      | 35.377±1.653 | 0.017±0.003 |
| SR Fine-tuning   | 0.993±0.004    | 45.706±2.169 | 0.005±0.002 | 0.973±0.005    | 42.158±6.626 | 0.007±0.001 | 0.957±0.006      | 40.654±7.651 | 0.014±0.004 |

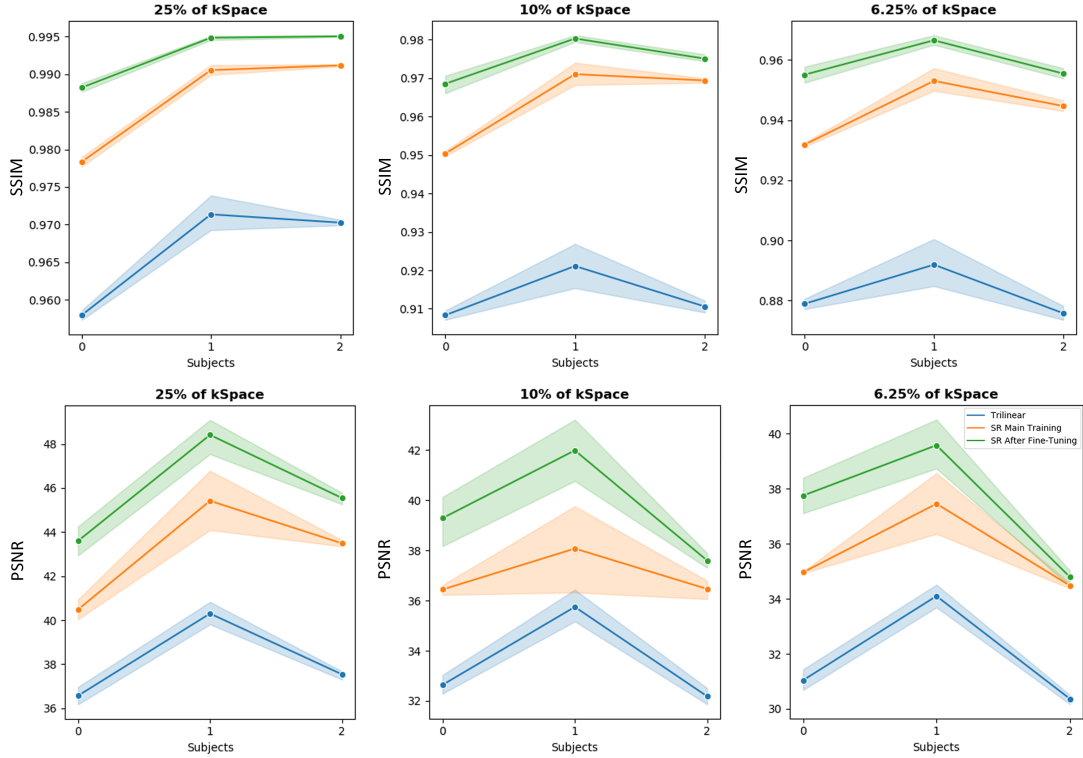


Figure 6: Line plot showing the mean and 95% confidence interval of the resultant SSIM and PSNR over the different time-points for each subject

In the presented approach, a 3D U-Net was used as the network model, which needs interpolation as a pre-processing step. Therefore the reconstructed images could be suffering from interpolation errors. As future work, network models such as SRCNN, which do not need interpolation, will be studied. In addition, image resolutions lower than the already investigated ones will be studied to check the network's limitations. Moreover, clinical interventions are performed with devices, such as needle, which are not present in the planning scan. The authors plan to extend this research in future by evaluating on images with such devices.

## Acknowledgements

This work was conducted within the context of the International Graduate School MEMORIAL at Otto von Guericke University (OVGU) Magdeburg, Germany, kindly supported by the European Structural and Investment Funds (ESF) under the programme "Sachsen-Anhalt WISSENSCHAFT Internationalisierung" (project no. ZS/2016/08/80646).

## References

- Bengio, Y., Goodfellow, I., Courville, A., 2017. Deep learning. volume 1. MIT press Massachusetts, USA:.
- Bernstein, M.A., King, K.F., Zhou, X.J., 2004. Handbook of MRI pulse sequences. Elsevier.
- Chatterjee, S., 2020. soumickmj/mrunder: Initial release. doi:10.5281/zenodo.3901455.
- Chatterjee, S., Breikopf, M., Sarasaen, C., Rose, G., Nürnberg, A., Speck, O., 2019. A deep learning approach for reconstruction of undersampled cartesian and radial data, in: ESMRMB 2019.
- Chatterjee, S., Prabhu, K., Pattadkal, M., Bortsova, G., Dubost, F., Mattern, H., de Bruijne, M., Speck, O., Nürnberg, A., 2020. Ds6: Deformation-aware learning for small vessel segmentation with small, imperfectly labeled dataset. arXiv preprint arXiv:2006.10802.
- Chaudhari, A.S., Fang, Z., Kogan, F., Wood, J., Stevens, K.J., Gibbons, E.K., Lee, J.H., Gold, G.E., Hargreaves, B.A., 2018. Super-resolution musculoskeletal mri using deep learning. *Magnetic resonance in medicine* 80, 2139–2154.
- Chen, Y., Shi, F., Christodoulou, A.G., Xie, Y., Zhou, Z., Li, D., 2018. Efficient and accurate mri super-resolution using a generative adversarial network and 3d multi-level densely connected network, in: International Conference on Medical Image Computing and Computer-Assisted Intervention, Springer. pp. 91–99.
- Choi, K., Fazekas, G., Sandler, M., Cho, K., 2017. Transfer learning for music classification and regression tasks. arXiv preprint arXiv:1703.09179.
- Çiçek, Ö., Abdulkadir, A., Lienkamp, S.S., Brox, T., Ronneberger, O., 2016. 3d u-net: learning dense volumetric segmentation from sparse annotation, in: International conference on medical image computing and computer-assisted intervention, Springer. pp. 424–432.
- Coupé, P., Manjón, J.V., Chamberland, M., Descoteaux, M., Hiba, B., 2013. Collaborative patch-based super-resolution for diffusion-weighted images. *NeuroImage* 83, 245–261.
- Dai, W., Xue, G.R., Yang, Q., Yu, Y., 2007. Transferring naive bayes classifiers for text classification, in: AAAI, pp. 540–545.
- Deka, B., Mullah, H.U., Datta, S., Lakshmi, V., Ganesan, R., 2020. Sparse representation based super-resolution of mri images with non-local total variation regularization. *SN Computer Science* 1, 1–13.
- Dong, C., Loy, C.C., He, K., Tang, X., 2014. Learning a deep convolutional network for image super-resolution, in: European conference on computer vision, Springer. pp. 184–199.
- Dong, C., Loy, C.C., Tang, X., 2016. Accelerating the super-resolution convolutional neural network, in: European conference on computer vision, Springer. pp. 391–407.
- Frid-Adar, M., Diamant, I., Klang, E., Amitai, M., Goldberger, J., Greenspan, H., 2017. Modeling the intra-class variability for liver lesion detection using a multi-class patch-based cnn, in: International Workshop on Patch-based Techniques in Medical Imaging, Springer. pp. 129–137.
- Frid-Adar, M., Diamant, I., Klang, E., Amitai, M., Goldberger, J., Greenspan, H., 2018. Gan-based synthetic medical image augmentation for increased cnn performance in liver lesion classification. *Neurocomputing* 321, 321–331.
- Gatys, L.A., Ecker, A.S., Bethge, M., 2016. Image style transfer using convolutional neural networks, in: Proceedings of the IEEE conference on computer vision and pattern recognition, pp. 2414–2423.
- Ghodrati, V., Shao, J., Bydder, M., Zhou, Z., Yin, W., Nguyen, K.L., Yang, Y., Hu, P., 2019. Mr image reconstruction using deep learning: evaluation of network structure and loss functions. *Quantitative imaging in medicine and surgery* 9, 1516–1527.
- Gu, Y., Zeng, Z., Chen, H., Wei, J., Zhang, Y., Chen, B., Li, Y., Qin, Y., Xie, Q., Jiang, Z., et al., 2020. Medsrgan: medical images super-resolution using generative adversarial networks. *Multimedia Tools and Applications* 79, 21815–21840.
- Hammernik, K., Klatzer, T., Kobler, E., Recht, M.P., Sodickson, D.K., Pock, T., Knoll, F., 2018. Learning a variational network for reconstruction of accelerated mri data. *Magnetic resonance in medicine* 79, 3055–3071.
- He, X., Lei, Y., Fu, Y., Mao, H., Curran, W.J., Liu, T., Yang, X., 2020. Super-resolution magnetic resonance imaging reconstruction using deep attention networks, in: Medical Imaging 2020: Image Processing, International Society for Optics and Photonics. p. 113132J.
- Huang, Y., Shao, L., Frangi, A.F., 2017. Simultaneous super-resolution and cross-modality synthesis of 3d medical images using weakly-supervised joint convolutional sparse coding, in: Proceedings of the IEEE Conference on Computer Vision and Pattern Recognition, pp. 6070–6079.
- Hyun, C.M., Kim, H.P., Lee, S.M., Lee, S., Seo, J.K., 2018. Deep learning for undersampled mri reconstruction. *Physics in Medicine & Biology* 63, 135007.
- Iqbal, Z., Nguyen, D., Hangel, G., Motyka, S., Bogner, W., Jiang, S., 2019. Super-resolution 1h magnetic resonance spectroscopic imaging utilizing deep learning. *Frontiers in oncology* 9.
- Isaac, J.S., Kulkarni, R., 2015. Super resolution techniques for medical image processing, in: 2015 International Conference on Technologies for Sustainable Development (ICTSD), IEEE. pp. 1–6.
- Jain, S., Sima, D.M., Sanaei Nezhad, F., Hangel, G., Bogner, W., Williams, S., Van Huffel, S., Maes, F., Smeets, D., 2017. Patch-based super-resolution of mr spectroscopic images: application to multiple sclerosis. *Frontiers in neuroscience* 11, 13.
- Johnson, J., Alahi, A., Fei-Fei, L., 2016. Perceptual losses for real-time style transfer and super-resolution, in: European conference on computer vision, Springer. pp. 694–711.
- Jung, H., Sung, K., Nayak, K.S., Kim, E.Y., Ye, J.C., 2009. k-t focuss: a general compressed sensing framework for high resolution dynamic mri. *Magnetic Resonance in Medicine: An Official Journal of the International Society for Magnetic Resonance in Medicine* 61, 103–116.
- Kavur, A.E., Gezer, N.S., Barış, M., Aslan, S., Conze, P.H., Groza, V., Pham, D.D., Chatterjee, S., Ernst, P., Özkan, S., et al., 2020. Chaos challenge-combined (ct-mr) healthy abdominal organ segmentation. *Medical Image Analysis*, 101950.
- Kim, Y.G., Kim, S., Cho, C.E., Song, I.H., Lee, H.J., Ahn, S., Park, S.Y., Gong, G., Kim, N., 2020. Effectiveness of transfer learning for enhancing tumor classification with a convolutional neural network on frozen sections. *Scientific Reports* 10, 1–9.
- Lateh, M.A., Muda, A.K., Yusof, Z.I.M., Muda, N.A., Azmi, M.S., 2017. Handling a small dataset problem in prediction model by employ artificial data generation approach: A review, in: Journal of Physics: Conference Series, p. 012016.
- Ledig, C., Theis, L., Huszár, F., Caballero, J., Cunningham, A., Acosta, A., Aitken, A., Tejani, A., Totz, J., Wang, Z., et al., 2017. Photo-realistic single image super-resolution using a generative adversarial network, in: Proceedings of the IEEE conference on computer vision and pattern recognition, pp. 4681–4690.
- Lee, K.H., He, X., Zhang, L., Yang, L., 2018. Cleannet: Transfer learning for scalable image classifier training with label noise, in: Proceedings of the IEEE Conference on Computer Vision and Pattern Recognition, pp. 5447–5456.

- Li, B., Yang, Q., Xue, X., 2009. Transfer learning for collaborative filtering via a rating-matrix generative model, in: Proceedings of the 26th annual international conference on machine learning, pp. 617–624.
- Liang, M., Du, J., Li, L., Xue, Z., Wang, X., Kou, F., Wang, X., 2020. Video super-resolution reconstruction based on deep learning and spatio-temporal feature self-similarity. *IEEE Transactions on Knowledge and Data Engineering*.
- Liu, C., Wu, X., Yu, X., Tang, Y., Zhang, J., Zhou, J., 2018. Fusing multi-scale information in convolution network for mr image super-resolution reconstruction. *Biomedical engineering online* 17, 1–23.
- Lustig, M., Donoho, D., Pauly, J.M., 2007. Sparse mri: The application of compressed sensing for rapid mr imaging. *Magnetic Resonance in Medicine: An Official Journal of the International Society for Magnetic Resonance in Medicine* 58, 1182–1195.
- Lustig, M., Santos, J.M., Donoho, D.L., Pauly, J.M., 2006. kt sparse: High frame rate dynamic mri exploiting spatio-temporal sparsity, in: Proceedings of the 13th annual meeting of ISMRM, Seattle.
- Lyu, Q., Shan, H., Xie, Y., Li, D., Wang, G., 2020. Cine cardiac mri motion artifact reduction using a recurrent neural network. *arXiv preprint arXiv:2006.12700*.
- Mahnken, A.H., Rieke, J., Wilhelm, K.E., 2009. CT-and MR-guided Interventions in Radiology, volume 22. Springer.
- Manjón, J.V., Coupé, P., Buades, A., Fonov, V., Collins, D.L., Robles, M., 2010. Non-local mri upsampling. *Medical image analysis* 14, 784–792.
- Misra, D., Crispim-Junior, C., Tougne, L., 2020. Patch-based cnn evaluation for bark classification, in: European Conference on Computer Vision, Springer. pp. 197–212.
- Pan, S.J., Yang, Q., 2009. A survey on transfer learning. *IEEE Transactions on knowledge and data engineering* 22, 1345–1359.
- Paszke, A., Gross, S., Massa, F., Lerer, A., Bradbury, J., Chanan, G., Killeen, T., Lin, Z., Gimelshein, N., Antiga, L., Desmaison, A., Kopf, A., Yang, E., DeVito, Z., Raison, M., Tejani, A., Chilamkurthy, S., Steiner, B., Fang, L., Bai, J., Chintala, S., 2019. Pytorch: An imperative style, high-performance deep learning library, in: Wallach, H., Larochelle, H., Beygelzimer, A., d'Alché-Buc, F., Fox, E., Garnett, R. (Eds.), *Advances in Neural Information Processing Systems* 32. Curran Associates, Inc., pp. 8024–8035.
- Perez, L., Wang, J., 2017. The effectiveness of data augmentation in image classification using deep learning. *arXiv preprint arXiv:1712.04621*.
- Pham, C.H., Ducournau, A., Fablet, R., Rousseau, F., 2017. Brain mri super-resolution using deep 3d convolutional networks, in: 2017 IEEE 14th International Symposium on Biomedical Imaging (ISBI 2017), IEEE. pp. 197–200.
- Plenge, E., Poot, D.H., Bernsen, M., Kotek, G., Houston, G., Wielopolski, P., van der Weerd, L., Niessen, W.J., Meijering, E., 2012. Super-resolution methods in mri: can they improve the trade-off between resolution, signal-to-noise ratio, and acquisition time? *Magnetic resonance in medicine* 68, 1983–1993.
- Qin, C., Schlemper, J., Caballero, J., Price, A.N., Hajnal, J.V., Rueckert, D., 2018. Convolutional recurrent neural networks for dynamic mr image reconstruction. *IEEE transactions on medical imaging* 38, 280–290.
- Ran, Q., Xu, X., Zhao, S., Li, W., Du, Q., 2020. Remote sensing images super-resolution with deep convolution networks. *Multimedia Tools and Applications* 79, 8985–9001.
- Ronneberger, O., Fischer, P., Brox, T., 2015. U-net: Convolutional networks for biomedical image segmentation, in: International Conference on Medical image computing and computer-assisted intervention, Springer. pp. 234–241.
- Rousseau, F., Initiative, A.D.N., et al., 2010. A non-local approach for image super-resolution using intermodality priors. *Medical image analysis* 14, 594–605.
- Sajjadi, M.S., Scholkopf, B., Hirsch, M., 2017. Enhancenet: Single image super-resolution through automated texture synthesis, in: Proceedings of the IEEE International Conference on Computer Vision, pp. 4491–4500.
- Sarasaen, C., Chatterjee, S., Nürnberger, A., Speck, O., 2020. Super resolution of dynamic mri using deep learning, enhanced by prior-knowledge, in: 37th Annual Scientific Meeting Congress of the European Society for Magnetic Resonance in Medicine and Biology, 33(Supplement 1): S03.04, S28–S29, Springer. doi:10.1007/s10334-020-00874-0.
- Shi, W., Caballero, J., Huszár, F., Totz, J., Aitken, A.P., Bishop, R., Rueckert, D., Wang, Z., 2016. Real-time single image and video super-resolution using an efficient sub-pixel convolutional neural network, in: Proceedings of the IEEE conference on computer vision and pattern recognition, pp. 1874–1883.
- Tang, Y., Shao, L., 2016. Pairwise operator learning for patch-based single-image super-resolution. *IEEE Transactions on Image Processing* 26, 994–1003.
- Tanno, R., Worrall, D.E., Ghosh, A., Kaden, E., Sotiropoulos, S.N., Criminisi, A., Alexander, D.C., 2017. Bayesian image quality transfer with cnns: exploring uncertainty in dmri super-resolution, in: International Conference on Medical Image Computing and Computer-Assisted Intervention, Springer. pp. 611–619.
- Tappen, M.F., Liu, C., 2012. A bayesian approach to alignment-based image hallucination, in: European conference on computer vision, Springer. pp. 236–249.
- Tsao, J., Boesiger, P., Pruessmann, K.P., 2003. k-t blast and k-t sense: dynamic mri with high frame rate exploiting spatiotemporal correlations. *Magnetic Resonance in Medicine: An Official Journal of the International Society for Magnetic Resonance in Medicine* 50, 1031–1042.
- Van Reeth, E., Tham, I.W., Tan, C.H., Poh, C.L., 2012. Super-resolution in magnetic resonance imaging: a review. *Concepts in Magnetic Resonance Part A* 40, 306–325.
- Wang, M., Deng, W., 2018. Deep visual domain adaptation: A survey. *Neuro-computing* 312, 135–153.
- Wang, S., Su, Z., Ying, L., Peng, X., Zhu, S., Liang, F., Feng, D., Liang, D., 2016. Accelerating magnetic resonance imaging via deep learning, in: 2016 IEEE 13th International Symposium on Biomedical Imaging (ISBI), IEEE. pp. 514–517.
- Wang, Z., Bovik, A.C., Sheikh, H.R., Simoncelli, E.P., 2004. Image quality assessment: from error visibility to structural similarity. *IEEE transactions on image processing* 13, 600–612.
- Wang, Z., Chen, J., Hoi, S.C., 2020. Deep learning for image super-resolution: A survey. *IEEE transactions on pattern analysis and machine intelligence*.
- Wang, Z., Simoncelli, E.P., Bovik, A.C., 2003. Multiscale structural similarity for image quality assessment, in: The Thirty-Seventh Asilomar Conference on Signals, Systems & Computers, 2003, Ieee. pp. 1398–1402.
- Wilson, G., Cook, D.J., 2020. A survey of unsupervised deep domain adaptation. *ACM Transactions on Intelligent Systems and Technology (TIST)* 11, 1–46.
- Yang, C.Y., Ma, C., Yang, M.H., 2014. Single-image super-resolution: A benchmark, in: European Conference on Computer Vision, Springer. pp. 372–386.
- Yu, X., Fernando, B., Ghanem, B., Porikli, F., Hartley, R., 2018. Face super-resolution guided by facial component heatmaps, in: Proceedings of the European Conference on Computer Vision (ECCV), pp. 217–233.
- Zeng, K., Zheng, H., Cai, C., Yang, Y., Zhang, K., Chen, Z., 2018. Simultaneous single-and multi-contrast super-resolution for brain mri images based on a convolutional neural network. *Computers in biology and medicine* 99, 133–141.
- Zhang, H., Yang, Z., Zhang, L., Shen, H., 2014. Super-resolution reconstruction for multi-angle remote sensing images considering resolution differences. *Remote Sensing* 6, 637–657.
- Zhang, Y., Wu, G., Yap, P.T., Feng, Q., Lian, J., Chen, W., Shen, D., 2012. Reconstruction of super-resolution lung 4d-ct using patch-based sparse representation, in: 2012 IEEE Conference on Computer Vision and Pattern Recognition, IEEE. pp. 925–931.
- Zhao, W., 2017. Research on the deep learning of the small sample data based on transfer learning, in: AIP Conference Proceedings, AIP Publishing LLC. p. 020018.
- Zhu, Y., Zhang, Y., Yuille, A.L., 2014. Single image super-resolution using deformable patches, in: Proceedings of the IEEE Conference on Computer Vision and Pattern Recognition, pp. 2917–2924.